Electronic supporting information for "THE EVOLUTION OF SURFACE STRUCTURE DURING SIMULATED ATMOSPHERIC AGEING OF NANO-SCALE COATINGS OF AN ORGANIC SURFACTANT AEROSOL PROXY".

S1. Experimental methods

Spin-coated films

Spin-coated films of the oleic acid-sodium oleate proxy were prepared for NR/GI-SAXS measurements by first dissolving these components as 1 wt % solutions in methanol. These solutions were then mixed in a 1:1 wt ratio to afford the coating solution. The silicon surfaces were prepared by exposure to ozone in an ozone surface steriliser (~15 min); 1 wash distilled water then a series of 4 washes with methanol, always finishing with a methanol wash and blowing dry nitrogen air over the surface. A spin coater (*Laurell WS-650-23*) was set to the desired rpm and a 100 µL aliquot of the coating solution was pipetted onto the centre of the spinning silicon substrate. After the initial coating step, the spin-coater was set to spin at 3000 rpm for 30 s to ensure the solvent had evaporated fully.

Film thickness can be controlled by adjusting the spinning speed during spin coating (Richardson et al., 2015). For GI-SAXS samples, methanol was added to the side of the disks during an additional step (3000 rpm, 30 s) in order to remove any ridge formation at the disk's edges – this can affect the GI-SAXS measurement.

Neutron Reflectometry

The INTER NR beamline uses pulsed neutrons of varying wavelengths and the measurement angle is kept constant: this was at 1.4 or 1.6° for kinetic/water uptake runs and full characterisations were performed by stitching together reflectivity curves measured at 0.5 and 2.3 °. This full Q-range was 0.007 – 0.282 Å^{-1}. The measurement returns a relationship between R and Q. Plots of R vs Q or RQ^4 vs Q are the most common way of presenting NR data and are what will be used in this study.

The FIGARO NR beamline uses a continuous flux of neutrons and a chopper arrangement to provide wavelengths between 2.2 And 20 Å and the measurement angle is constant at 0.7 and 3.9 ° for the low and high angle settings, respectively (unless otherwise stated). The Q-range was 0.008 – 0.354 Å^{-1}.

NR measurements take longer to carry out than similar synchrotron X-ray techniques such as GI-SAXS, where scattering patterns are typically measured in seconds. This is due to the difference in flux between the neutron and X-ray sources. Typical NR measurements for full characterisations were 30-180 min. Data collected at the INTER beamline were collected in event mode and grouped into suitable time slices after the measurement. The NR data from each time slice and be extracted and fitted. For kinetic and water uptake runs we chose between 20 – 120 min time slices, which represented a balance between the need for well-resolved NR curves and a reasonable time resolution to follow structural changes. This low time resolution compared with GI-SAXS would result in some averaging of the NR curve over that 20 min time period. This would introduce some uncertainty in the model fitting, unavoidable with this experiment. Despite this, changes happened sufficiently slowly so that we could distinguish trends in the fitted parameters (see section 1.4, main text). In all cases, the model fit well with the data, supporting the assumption that little changed during these fitted time intervals.

Grazing-incidence small-angle X-ray scattering (GI-SAXS)

In GI-SAXS the scattered intensity (I) is a function of Q (see Eq. 2, main text). The spacing between equivalent scattering planes (d) is related to Q by applying Bragg's law ($d= \lambda/2\sin(\theta)$) to Eq. 2 (main text):

$$d = \frac{2\pi}{Q}$$

(S1)

The d-spacing can be used to determine the spacing between lamellar stacks formed by our samples in this study, as has been done before on a similar system (Milsom et al., 2021).

The orientation of the lamellar stacks can be inferred by variations in the azimuthal intensity profile at the lamellar peak Q position. An increase in I in the specular direction (*i.e.* scattering in the x-z plane in Fig. 1, main text) is consistent with a repeating structure that is oriented parallel to the surface. A diffuse scattering ring is consistent with random orientations.

Samples were mounted vertically and measured on the I22 beamline at the Diamond Light Source (UK) with X-rays at 14 keV energy and a 0.4° angle of incidence. Scattering patterns were measured for 1 s per frame over a Q-range of 0.007 – 0.5 Å^{-1}.

Offline GI-SAXS measurements were made using a *Xenocs Xeuss 2.0* equipped with a micro-focus Cu Kα source. Each pattern collection was 15 minutes. A more detailed description of the offline GI-SAXS setup is provided in sect. S4.

Ozonolysis

Ozonolysis experiments for time-sliced runs at INTER were carried out by passing dry oxygen through a UV pen-ray ozoniser (Ultraviolet Products Ltd, Cambridge, UK) and then to the sample chamber in which the sample was placed. The concentration of ozone was calibrated offline by UV spectroscopy by monitoring the absorption band of ozone at 254 nm and using the absorption cross-section ($(1.14 \pm 0.08) \times 10^{-17}$ cm^2) (Mauersberger et al., 1986). The ozone concentration was in the range of 126 – 4020 ppb and was varied by exposing oxygen to different amounts of UV light and varying the oxygen flow rate (which was varied between 0.4 – 1.2 L min^{-1}). An additional ozoniser was used to reach the highest ozone concentration. Previous experience with this self-assembled system has shown that it is necessary to have a high ozone concentration to observe an appreciable decay in the timeframe of a beamline experiment (Milsom et al., 2021).

Film oxidation at the FIGARO beamline followed the same procedure as above, without the additional ozoniser and an oxygen flow rate of 0.2 L min^{-1}. The ozone concentration was calculated to be 40 ppm. This was to ensure the film was thoroughly oxidised before humidity change experiments demonstrating differences in lamellar phase water uptake (see main text).

Humidity experiments

Humidity experiments at INTER were carried out using a Raspberry Pi (RPi) humidity control system. The RPi controlled two air pumps – one which pumped air through a bubbler filled with D$_2$O, the other pumping ambient air. The RPi achieved the target relative humidity (RH) by regulating the wet and dry air pumps. The two air flows were then mixed before entering the sample chamber. We used D$_2$O due to its larger SLD compared to H$_2$O, which provides better contrast and thus more information about the film structure.

Humidity experiments at FIGARO were carried out by mixing dry and wet (D_2O) flows of N_2 through the chamber. RH was increased and decreased in increments of ~ 20 % by using pre-calibrated air flows.

GI-SAXS humidity experiments differed slightly in that a different sample chamber was used and wet/dry air flows were regulated by mass flow controllers. RH was monitored by an RPi system as for the NR experiments.

NR model fitting

A layer model based on prior knowledge of sample parameters, such as substrate, incident medium (air) and possible film compositions is initially constructed and the reflectivity calculated using bespoke software (see below). The refinement of this initial model yields information about structural parameters (mostly thickness, density/composition and roughness of each layer in the model). These values are the corroborated and complemented by information obtained by other techniques, such as GI-SAXS and optical microscopy in this study.

The scattering process gives rise to (thickness) oscillations, which are a consequence of constructive and destructive interference arising from the coherent superposition of scattered neutrons from each interface. This coherent interference however, is spatially limited to the maximum coherence length of the incident neutrons, which is of the order of tens of microns (Majkrzak et al., 2014; Richardson et al., 1997). If lateral variation larger than the coherence of the neutrons occurs, then reflectivities from the different regions are added incoherently (i.e. by summing) in the scattering process. A model reflecting such a situation, where two or more distinct structures are present on the surface, with domains larger than the neutron coherence length, is referred to as "mixed area model".

For all fits performed in this study a mixed area model was selected, where the area illuminated by the neutron beam has regions of different interfacial structures (see Fig. 1 for a schematic representation, main text). This model, consisting of a lamellar stack region and an amorphous film region, fit the best to all the films probed in this study. This was backed up by determination of the Bayesian evidence for each model, complementary optical microscopy and GI-SAXS (see main text, sect. S5 and S6).

The lamellar stack model component comprised of two lipid layers (containing d_{34}-OA and sodium oleate) with roughness, number of stacks (lipid bilayers) and SLD allowed to vary during the fitting procedure. An additional D_2O layer between the stacks was included for humidification/dehumidification experiment model fitting. The amorphous film model component was represented as one layer with thickness, roughness and SLD allowed to vary. The relative amount of specular reflection from each of these components is obtained by varying a scale factor applied to each component. The contribution of each model component was scaled by their respective scale factors to afford the final model reflectivity curve. For the data collected at ISIS the total scale factor (sum of the scale factors from the lamellar and amorphous film regions) was constrained to be approximately what was measured for initial film characterisations (original scale factor plus or minus 0.02, where the critical edge could be seen at low-Q). Data collected at ILL were scaled so that the total scaling factor was 1.0 and fits were constrained accordingly.

MCMC sampling enabled us to determine the uncertainty in each varied model parameter by estimating a probability distribution for each. We could then illustrate the range of SLD profiles and model fits consistent with the experimental data. Details of the implementation of the MCMC method are in sect. S5.

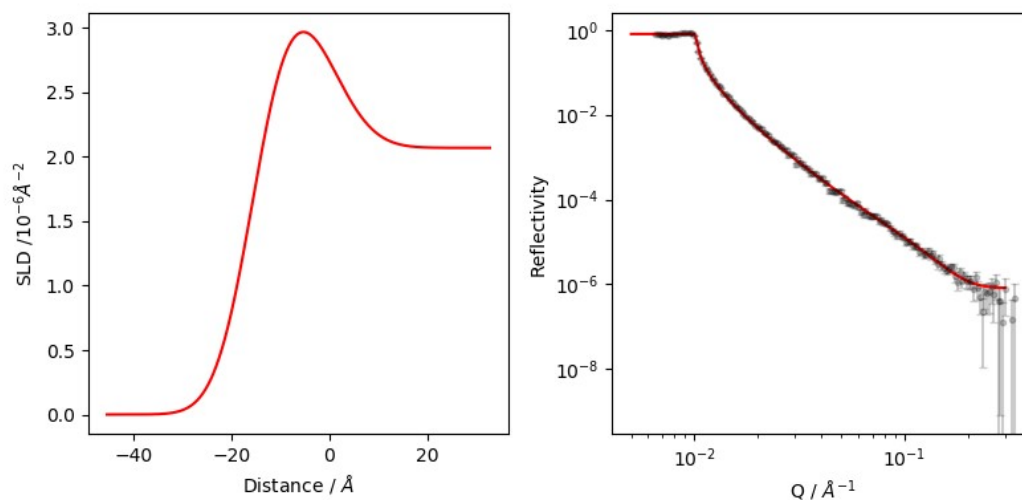## S2. Neutron reflectometry of bare silicon substrates

Figure S1. The NR curve and resulting SLD profile of one of the bare substrates (disk A) deposited on for the films presented in Fig. 4 of the main text.

Figure S2. The NR curve and resulting SLD profile of one of the bare substrates (block P60) deposited on for the films presented in Fig. 1 & 4 of the main text.

The silicon substrate roughness and the native SiO_2 layer thickness and roughness were determined for samples measured on INTER at ISIS by measuring an NR curve and fitting an interfacial model to it.

Si substrate roughness for one of the disks (disk A) was 7 Å and the thickness and roughness of the SiO_2 layer was 16 Å and 6 Å, respectively (Fig. S1). X-ray reflectometry was also carried out on this disk and returned 4 Å Si roughness and a SiO_2 layer thickness and roughness of 9 Å and 9 Å, respectively.

Si substrate roughness for the other substrate (block P60) was 2 Å and the thickness and roughness of the SiO_2 layer was 10 Å and 5 Å, respectively (Fig. S2).
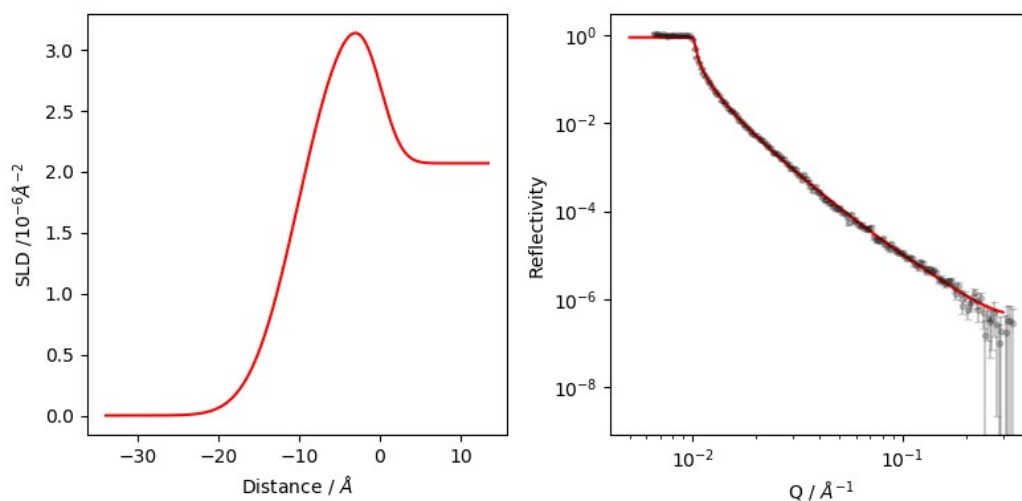
SiO$_2$ layer thickness was determined to be 11 Å for the substrates used on FIGARO at the ILL.
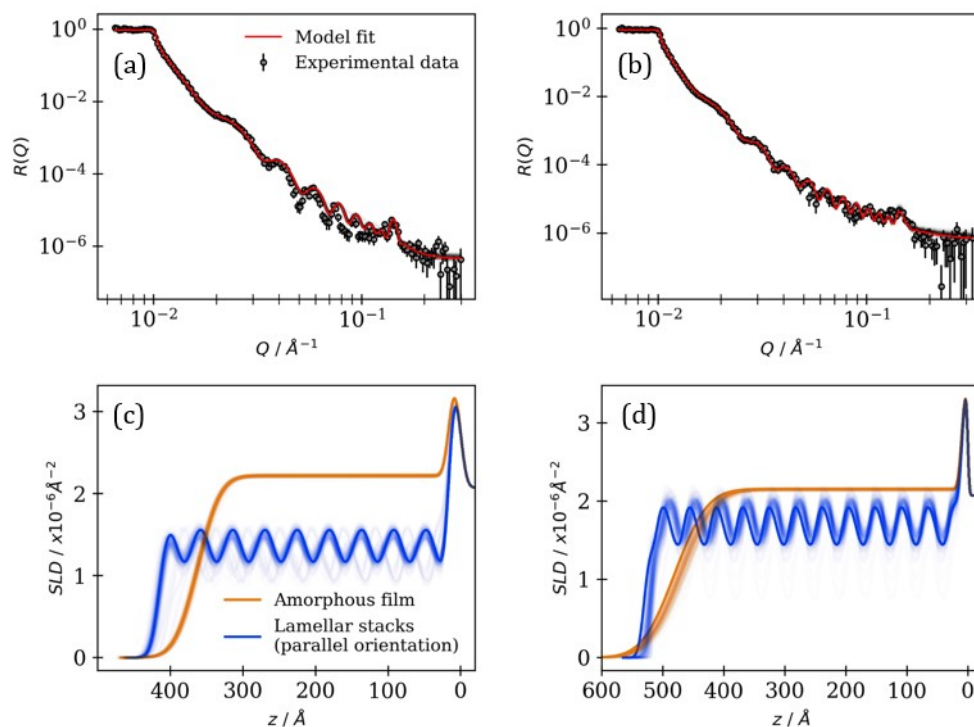
S3. Initial fits of spin-coated films

Figure S3.R vs Q curves of films coated at 2000 (a) and 1000 (b) rpm on the INTER instrument at ISIS. Model fits are presented along with 200 curves randomly sampled from the Markov Chains stored after the MCMC sampling procedure (black curves). SLD profiles corresponding to the amorphous film and lamellar stack region are presented below their relevant R vs Q curve ((c) and (d)). z is the distance from the substrate. 200 samples from the MCMC sampling procedure are presented.
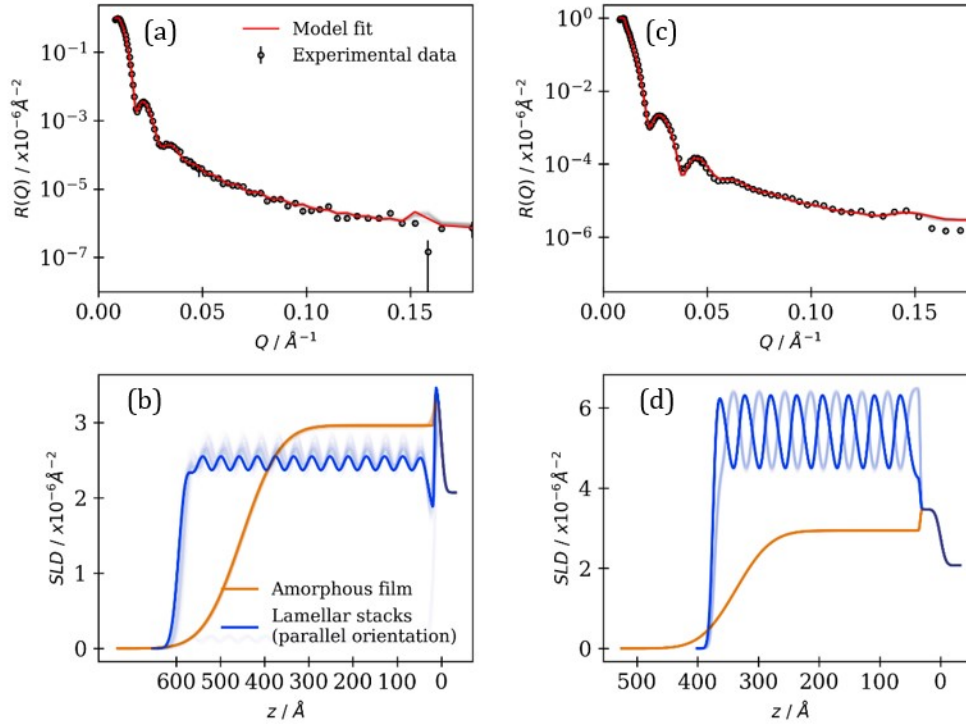
Figure S4. R vs Q curves of films coated at 2000 (a) and 4000 (c) rpm on the FIGARO instrument at the ILL. Model fits are presented along with 50 curves randomly sampled from the Markov Chains stored after the MCMC sampling procedure (black curves). SLD profiles corresponding to the amorphous film and lamellar stack region are presented below their relevant R vs Q curve ((b) and (d)). z is the distance from the substrate. 50 samples from the MCMC sampling procedure are presented.

The model fits presented in Fig. S3 (ISIS) and Fig. S4 (ILL) correspond to the fits summarised in table 1 of the main text.

S4. Further details of the offline GI-SAXS measurement

The scattering pattern was measured using a Pilatus 300k detector with a pixel size of 0.172 mm x 0.172 mm mounted on a translatable stage. The sample to detector distance for these samples 1.185 m and the detector was translated vertically and the images combined to form a virtual detector without gaps between the detector chips. Each image collection was 15 minutes. The sample chamber was filled with flowing dry nitrogen.

S5. Details of the MCMC and nested sampling procedures

Markov-Chain Monte Carlo (MCMC) sampling of the model parameter space was achieved by using the *CurveFitter* object in the *refnx* Python package (Nelson and Prescott, 2019). This curve fitting object used the ensemble sampler in the *emcee* Python package to sample the parameter space for a given NR model and data (Foreman-Mackey et al., 2013). Essentially, a chain is initialised with a parameter set sampled from the prior probability distribution of each parameter. In this case, the model was first fitted to the data with a differential evolution algorithm to find the parameter set that returns the best fit to the data.

The initial chains (parameter sets) were then created by sampling from a small Gaussian "ball" distribution created by adding some noise to the optimised parameters. These chains are referred to as walkers. At each step of the algorithm, a new parameter set is proposed and the likelihood of that step being accepted depends on how well the model fits to the data. The result is that walkers will find then move around an equilibrium region of the parameter space, each step being saved to the "chain" of parameter sets associated with each walker. Being at equilibrium, one can extract probability distributions for each model parameter. One can also take a number of samples from each chain and plot the model output, illustrating the distribution of model outputs consistent with the data (*e.g.* Fig. S4).

In this study, 200 walkers were initiated from the parameter set optimised with the differential evolution algorithm. An initial burn-in phase of 400 steps was used in order for the walkers to reach the equilibrium region of the parameter space. These steps were discarded from the chain before the production run was initiated. For this run, every 100th sample was saved and this was done 15 times. Therefore 3000 samples (200 * 15) were taken of the parameter space.

The principles behind the use of the *dynesty* python package are presented in detail by Speagle *et al.* (Speagle, 2020). Essentially, a number of live points (parameter sets) are drawn from the prior probability distribution for each parameter. In this case, we used 500 live points. Each point has a likelihood function (goodness-of-fit) evaluated. The point with the lowest likelihood is discarded and a new point with a higher likelihood is sampled. This is iterated until some stopping criterion is achieved. The stopping criterion in this case is when the contribution to the evidence of the remaining parameter volume compared to the total evidence from all samples is less than a threshold value. In this case, a value of 0.01 was
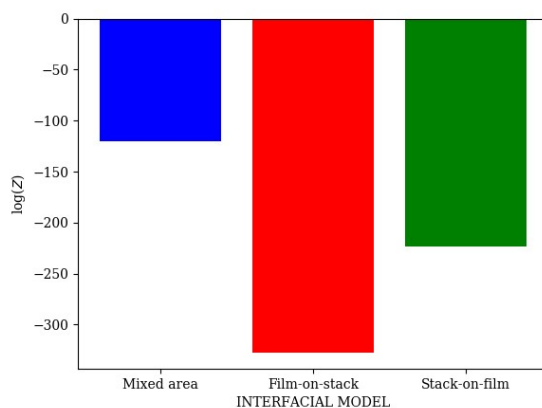
used (*dlogz* argument in the *run_nested* function of the *NestedSampler* object).

Figure S5. The log-evidence (Z) determined for each proposed model for the film coated at 2000 rpm, using the nested sampler available in the dynesty Python package (Speagle, 2020).

Three interfacial models were proposed: (i) Mixed area – regions of amorphous film and lamellar stacks; (ii) Film-on-stack – where an amorphous film is on top of a lamellar stack layer (air | film | lamellar stack | SiO_2 | Si); (iii) Stack-on-film – where a lamellar stack layer is on top of an amorphous film layer (air | lamellar stack | film | SiO_2 | Si). The nested sampling procedure was carried out for each of these proposed models.

It is evident from the plot of log(Z) vs interfacial model that the mixed area model is the one most suited to fit these datasets Fig. S5.

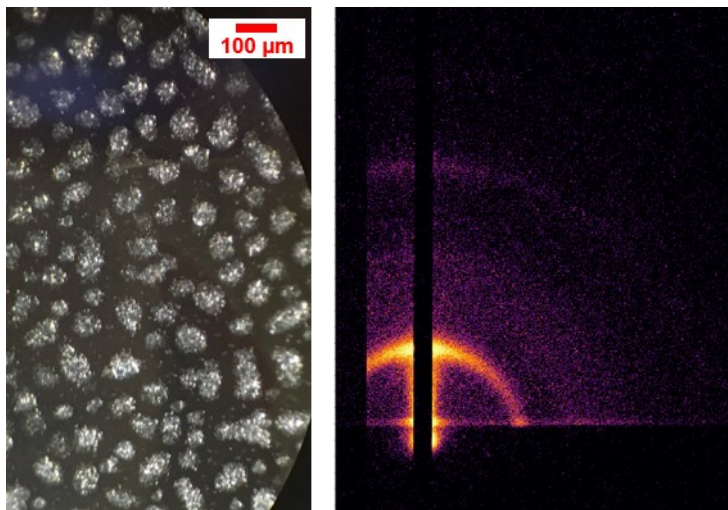## S6. Offline GI-SAXS pattern and microscopy of a spin-coated film

Figure S6. Optical microscopy image (left) and 2-D GI-SAXS pattern (right) of a film deposited on a silicon substrate.

A separate film was spin-coated offline (away from the beamline) and a GI-SAXS measurement taken (Fig. S6(left-hand)). This pattern exhibited a diffuse scattering ring corresponding to a lamellar phase bilayer. Scattering in the specular direction (vertical direction in Fig. S6(right-hand)) is more intense compared to the rest of the scattering peak. This means that there is a degree of parallel orientation of lamellar stacks, as demonstrated by synchrotron GI-SAXS and NR experiments in the main text.
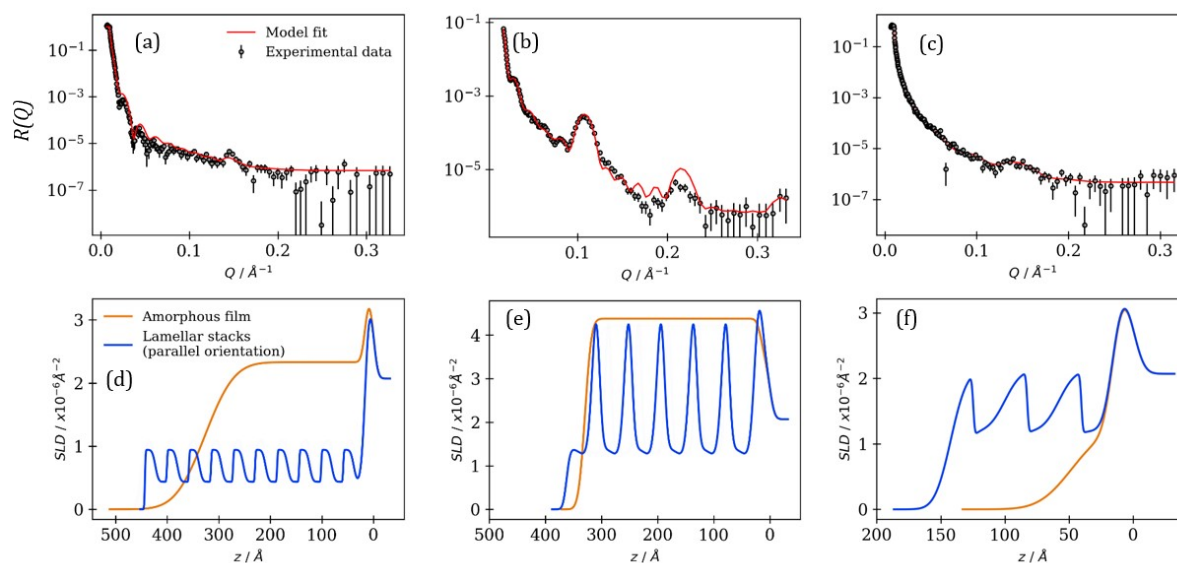
S7. Changes to the NR curve during ageing

Figure S7. NR curves and model fits ((a) – (c)) and corresponding SLD profiles ((d) – (f)) for a film coated at 2000 rpm. These curves are stitched together measurements at low and high angles (0.5 and 2.3 °, respectively). (a) and (d): characterisation after ~ 700 min ozone exposure (4020 ppb). (b) and (e): characterisation after humidification to ~ 90 % RH. (c) and (f): characterisation after dehumidification to ~ 5 % RH.

Full high- and low-angle NR measurements demonstrate how the structure of the film changes with exposure to ozone and humidity. A Bragg peak is visible throughout the experiments (see peak at ~ 0.14 Å⁻¹ in NR curves in Fig. S7). There is a visible shift of the Bragg peak at high RH (90 %) to ~ 0.1 Å⁻¹ (Fig. S7(b)). Note also that the critical edge (maximum R region at low Q) is lower at high RH compared with the two dry measurements (compare Fig. S7(b) to Fig. S7(a) and (c)). This is due to increased off-specular scattering corresponding to some lateral coherence in the surface structure (see section S7) (Dalgliesh, 2002; Hafner et al., 2021). At the end of the ageing experiment, the film is not as uniform and homogeneous as before. There is a lack of clear fringes and the model fit returns a very rough film and a lamellar region with 3 stacks parallel to the surface.
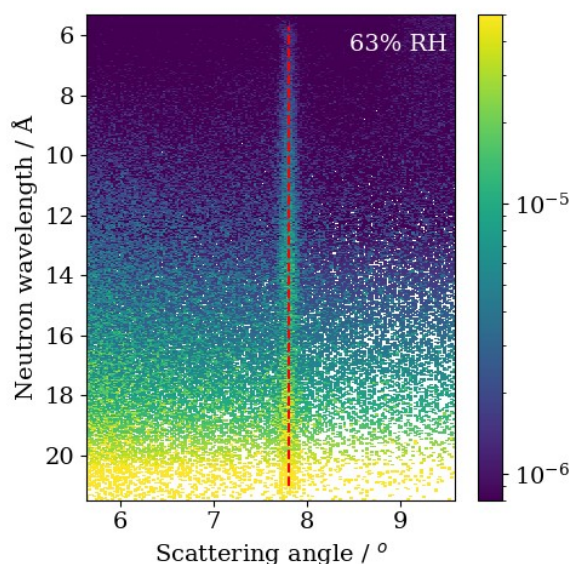
S8. Off-specular scattering

Figure S8. Off specular scattering observed from a film coated at 4000 rpm. Measurement at a high angle (3.9 °). The dashed red line indicates the specular direction.

A change in the off-specular scattering measured at a high incident angle (3.9 °) was not observed at an intermediate humidity (63 % RH) (Fig. S8, compare with Fig. 4(a) and (c) in the main text). A diagonal Bragg sheet is not observed neither is there an increase in scattered intensity expected if D_2O, which strongly scatters neutrons, is taken up by the lamellar sheets. There is therefore no significant water uptake by the film at this relative humidity (compared with the same measurement on the same film at high humidity in Fig. 4(c) of the main text).
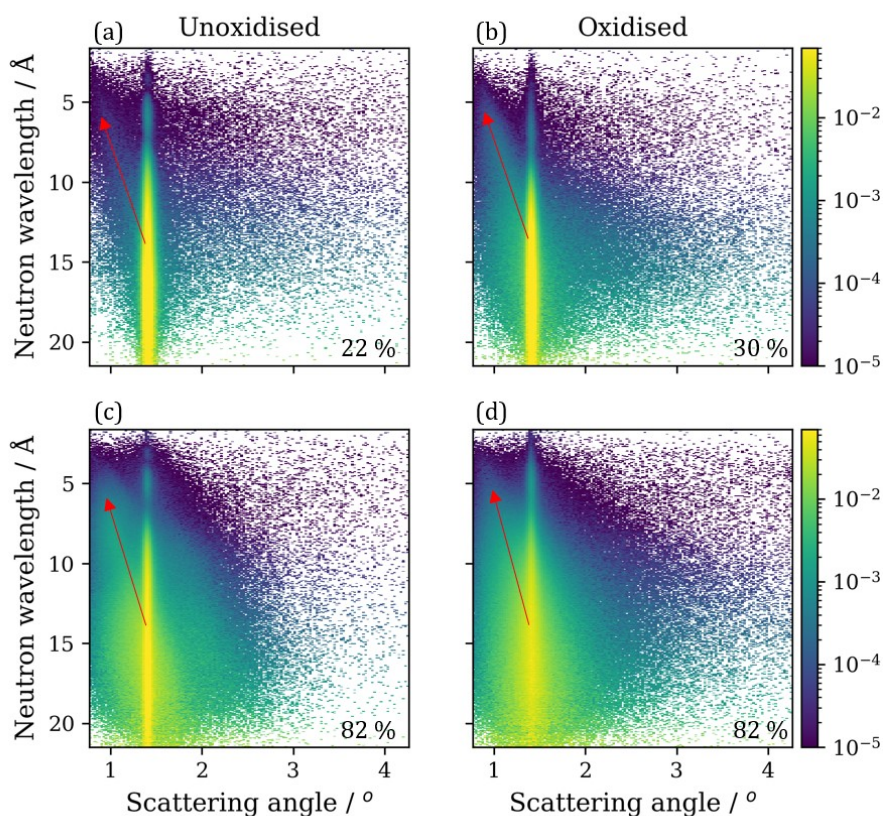
Figure S9. Off-specular scattering measured at 0.7 ^{o}, plotted as neutron wavelength vs scattering angle. These correspond to the same films presented in Fig. 4 in the main text, where the higher angle measurements are presented. A red arrow corresponding to the off-specular scattering around the critical edge (Yoneda scattering) is drawn on each plot. Relative humidity (%) is presented at the bottom right of each plot. (a) and (b) are measurements at low humidity for an unoxidised and oxidised film, respectively. (c) and (d) are the same films measured at high relative humidity.

Off-specular scattering measurements were carried out at a low angle (0.7 ^{o}), covering the critical edge observed at low-Q. Off-specular scattering corresponding to in-plane correlations in the surface structure is evident for films at low RH (< 35 %) (see the diagonal "streak" of intensity in Fig. S9 (a) & (b)). There is a marked increase in this off-specular signal at high humidity, which is consistent with de-wetting from the surface as has been observed for a the de-wetting of a polymer film (Castel et al., 2020). This increased off-specular signal explains the decrease in the critical edge observed in the specular 1-D NR data presented at high RH (see Fig. 4(e) in the main text – maximum R < 1 at low-Q).

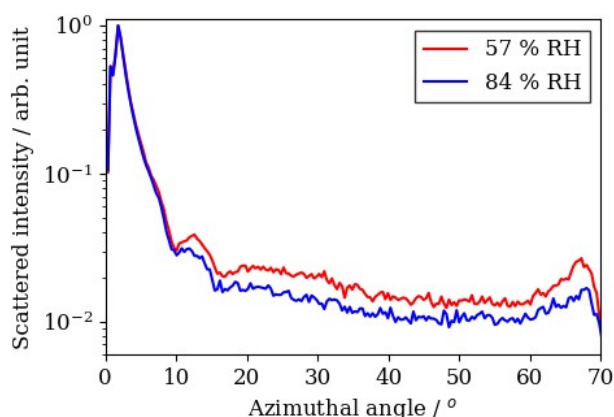## S9. Synchrotron GI-SAXS analysis at low and high humidity

Figure S10. 1-D Scattered intensity vs azimuthal angle for the lamellar phase Bragg peak position ($Q \sim 0.14$ Å^{-1}) derived from the 2-D GI-SAXS patterns presented in Fig. 5 of the main text. These intensities are sums of ± 70 ^{0} assuming azimuthal symmetry about the line defined by the reflected beam.

Performing an azimuthal integration around the lamellar phase Bragg peak position (~ 0.14 Å^{-1}) allows the ratio between specular and diffuse scattered intensity ($I_{specular}/I_{diffuse}$) to be calculated. In this case, "specular" was defined as up to an angle of 0 – 17 ^{o} with "diffuse" being all angles greater than 17 ^{o}. Note that at angles greater than ~ 70 ^{o} from the line defined by the reflected beam returned close to no scattering because of the physical barrier the silicon disk was to scattered X-rays in this particular experiment (see 2-D images in Fig. 5, main text, for an illustration of this). We assumed azimuthal symmetry about the reflected beam and summed scattered intensities together (Fig. S10).

References

Castel, A., Gutfreund, P., Cabane, B. and Rharbi, Y.: Stability of fluid ultrathin polymer films in contact with solvent-loaded gels for cultural heritage, Langmuir, 36(42), 12607–12619, doi:10.1021/acs.langmuir.0c02162, 2020.

Dalgliesh, R.: Application of off-specular scattering of X-rays and neutrons to the study of soft matter, Curr. Opin. Colloid Interface Sci., 7(3–4), 244–248, doi:10.1016/S1359-0294(02)00054-7, 2002.

Foreman-Mackey, D., Hogg, D. W., Lang, D. and Goodman, J.: emcee : The MCMC Hammer , Publ. Astron. Soc. Pacific, 125(925), 306–312, doi:10.1086/670067, 2013.

Hafner, A., Gutfreund, P., Toperverg, B. P., Jones, A. O. F., de Silva, J. P., Wildes, A., Fischer, H. E., Geoghegan, M. and Sferrazza, M.: Combined specular and off-specular reflectometry: elucidating the complex structure of soft buried interfaces, J. Appl. Crystallogr., 54(3), 924–948, doi:10.1107/S1600576721003575, 2021.

Majkrzak, C. F., Metting, C., Maranville, B. B., Dura, J. A., Satija, S., Udovic, T. and Berk, N. F.: Determination of the effective transverse coherence of the neutron wave packet as employed in reflectivity investigations of condensed-matter structures. I. Measurements, Phys. Rev. A, 89(3), 033851, doi:10.1103/PhysRevA.89.033851, 2014.

Mauersberger, K., Barnes, J., Hanson, D. and Morton, J.: Measurement of the ozone absorption cross-section at the 253.7 nm mercury line, Geophys. Res. Lett., 13(7), 671–673, doi:10.1029/GL013i007p00671, 1986.

Milsom, A., Squires, A. M., Woden, B., Terrill, N. J., Ward, A. D. and Pfrang, C.: The persistence of a proxy for cooking emissions in megacities: a kinetic study of the ozonolysis of self-assembled films by simultaneous small and wide angle X-ray scattering (SAXS/WAXS) and Raman microscopy, Faraday Discuss., 226, 364–381, doi:10.1039/D0FD00088D, 2021.

Nelson, A. R. J. and Prescott, S. W.: Refnx: Neutron and X-ray reflectometry analysis in python, J. Appl. Crystallogr., 52, 193–200, doi:10.1107/S1600576718017296, 2019.

Richardson, R. M., Webster, J. R. P. and Zarbakhsh, A.: Study of Off-Specular Neutron Reflectivity Using a Model System, J. Appl. Crystallogr., 30(6), 943–947, doi:10.1107/S0021889897003440, 1997.

Richardson, S. J., Staniec, P. A., Newby, G. E., Rawle, J. L., Slaughter, A. R., Terrill, N. J., Elliott, J. M. and Squires, A. M.: Glycerol prevents dehydration in lipid cubic phases, Chem. Commun., 51, 11386–11389, doi:10.1039/c5cc03771a, 2015.

Speagle, J. S.: DYNESTY: a dynamic nested sampling package for estimating Bayesian posteriors and evidences, Mon. Not. R. Astron. Soc., 493(3), 3132–3158, doi:10.1093/MNRAS/STAA278, 2020.